

# DifAttack++: Query-Efficient Black-Box Adversarial Attack via Hierarchical Disentangled Feature Space in Cross Domain

Jun Liu<sup>1</sup> · Jiantao Zhou<sup>\*1</sup> · Jiandian Zeng<sup>2</sup> · Jinyu Tian<sup>3</sup> · Zheng Li<sup>1</sup>

Received: date / Accepted: date

**Abstract** This work investigates efficient score-based black-box adversarial attacks with a high Attack Success Rate (**ASR**) and good generalizability. We design a novel attack method based on a hierarchical Disentangled Feature space, called **DifAttack++**, which differs significantly from the existing ones operating over the entire feature space. Specifically, DifAttack++ firstly disentangles an image’s latent feature into an Adversarial Feature (**AF**) and a Visual Feature (**VF**) via an autoencoder equipped with our specially designed Hierarchical Decouple-Fusion (**HDF**) module, where the AF dominates the adversarial capability of an image, while the VF largely determines its visual appearance. We train such two autoencoders for the clean and adversarial image domains (i.e., cross-domain) respectively to achieve image reconstructions and feature disentanglement, by using pairs of clean images and their Adver-

sarial Examples (**AEs**) generated from available surrogate models via white-box attack methods. Eventually, in the black-box attack stage, DifAttack++ iteratively optimizes the AF according to the query feedback from the victim model until a successful AE is generated, while keeping the VF unaltered. Extensive experimental results demonstrate that our DifAttack++ leads to superior ASR and query efficiency than state-of-the-art methods, meanwhile exhibiting much better visual quality of AEs. The code is available at <https://github.com/csjunjun/DifAttack.git>.

**Keywords** Black-box Adversarial Attack · Query-Efficient · Disentanglement · Hierarchical

## 1 Introduction

Adversarial Examples (**AEs**) refer to images that deceive Deep Neural Networks (**DNNs**) by incorporating imperceptible perturbations onto clean images. Although AEs pose a security threat to many DNNs, it has also been observed that meticulously crafted AEs are beneficial for evaluating and improving the robustness of DNNs Dong et al (2020); Croce and Hein (2020b); Tian et al (2021); Wu et al (2022); Kazemi et al (2023); Li et al (2024), and can even be employed for the privacy protection Liu et al (2023, 2024a). The methods for generating AEs can be roughly classified into three categories based on the information of victim DNNs available to the attacker. The first category is the white-box attack Dong et al (2018); Croce and Hein (2020a); Zhang et al (2021), in which the attacker has access to the architecture and weights of the victim model. The second category is called the black-box attack, where the attacker can only obtain the model’s output. The case where the model’s output contains

Jun Liu<sup>1</sup>  
E-mail: yc07453@um.edu.mo

Jiantao Zhou<sup>\*1</sup>  
E-mail: jtzhou@um.edu.mo

Jiandian Zeng<sup>2</sup>  
E-mail: jiandian@bnu.edu.cn

Jinyu Tian<sup>3</sup>  
E-mail: jytian@must.edu.mo

Zheng Li<sup>1</sup>  
E-mail: yc27908@um.edu.mo

<sup>1</sup> State Key Laboratory of Internet of Things for Smart City, Department of Computer and Information Science, University of Macau

<sup>2</sup> Institute of Artificial Intelligence and Future Networks, Beijing Normal University

<sup>3</sup> School of Computer Science and Engineering, Macau University of Science and Technology

both categories and scores is known as a score-based black-box attack, while the situation where only categories are included is named a decision-based black-box attack [Brendel et al \(2018\)](#). The third category refers to the gray-box attack [Guo et al \(2018\)](#), where the attacker can obtain models’ knowledge that falls between white-box attacks and black-box attacks. Given that contemporary potent classification APIs, e.g., [Google \(2024\)](#); [Imagga \(2024\)](#), generally provide image prediction categories alongside scores, this work primarily focuses on the practical score-based black-box attacks.

We observe that State-Of-The-Art (**SOTA**) score-based black-box attack methods predominantly exhibit two aspects that can be improved. **On the one hand**, prior techniques that seek AEs by optimizing image features usually operate within the entire feature space, such as AdvFlow [Mohaghegh Dolatabadi et al \(2020\)](#), TREMBA [Huang and Zhang \(2020\)](#) and CGA [Feng et al \(2022\)](#), without embracing the disentanglement of adversarial capability and visual characteristics in the image feature. Optimizing the entire feature of images could result in substantial pixel perturbations that will encounter truncation by the predefined distortion constraint, thus diminishing the optimization efficacy of the features and eventually increasing query numbers. Another possible chain reaction is the decrease in the Attack Success Rate (**ASR**) caused by the limited query numbers. Although there are a few black-box methods that achieve leading ASR and query efficiency, the visual quality of their generated AEs is often unsatisfactory and quite perceptible. For instance, SquareAttack [Andriushchenko et al \(2020\)](#) usually produces AEs filled with colored stripes and squares. To improve the unsatisfactory ASR and query efficiency, meanwhile maintaining the visual quality of AEs, our DifAttack++ disentangles an image’s latent feature into an Adversarial Feature (**AF**) and a Visual Feature (**VF**), where the former dominates the adversarial capability of an image, while the latter largely determines its visual appearance. Afterward, the AF is iteratively optimized according to the query feedback, while keeping the VF unaltered.

**On the other hand**, some score-based attack techniques including P-RGF [Cheng et al \(2019\)](#) and GFCS [Lord et al \(2022\)](#), exploit the gradients from local white-box surrogate models to update AEs during each query. These methods are effective when image categories of the training dataset for surrogate models and the victim model are the same, namely a **close-set** black-box attack scenario analogy to the close-set recognition setting [Vaze et al \(2021\)](#); [Shao et al \(2022\)](#). When it comes to an **open-set** black-box attack, wherein the training dataset of the victim model is unknown, the effective-

ness of these methods declines dramatically, as the possible incongruence between the output categories of surrogate models and the victim model hampers the calculation of gradients from surrogate models. Although there are other approaches, such as SimBA [Guo et al \(2019a\)](#), CGA [Feng et al \(2022\)](#) and SquareAttack [Andriushchenko et al \(2020\)](#), which are workable in both open-set and close-set scenarios, they still face challenges in terms of the query efficiency, ASR or severe degradation of image quality. In contrast, our DifAttack++ circumvents the need to compute gradients of surrogate models when updating AEs to be queried. Instead, before embarking on querying the victim model, we leverage AEs generated by performing white-box attack methods on surrogate models to learn how to extract a disentangled AF and VF from the image’s latent feature, which enables DifAttack++ to more effectively conduct black-box attacks in open-set scenarios. The efficiency of DifAttack++ in open-set scenarios can be attributed to the fact that the disentangled feature space for optimizing AEs is also responsible for the image reconstruction task, which means that an image can still be reconstructed into its original form with a minimal loss after being mapped into our disentangled feature space. However, the feature space in other methods, such as TREMBA [Huang and Zhang \(2020\)](#) and CGA [Feng et al \(2022\)](#), is directly used to generate adversarial perturbations that are tightly bound to the data distribution of the training dataset. The latent feature for image reconstructions in DifAttack++ has better generalizability to unknown datasets than the feature space learned from adversarial perturbation distributions of a specific dataset. In addition, DifAttack++ owns the flexibility to selectively harness surrogate models, e.g., in closed-set scenarios, generating transferable AEs as the starting point for the query attack.

More specifically, in DifAttack++, we first train two distinct autoencoders equipped with the designed Hierarchical Decouple-Fusion (**HDF**) module to achieve image reconstructions and to disentangle AFs as well as VFs from images’ latent features. In the training stage, our proposed feature interchange operations in Cross-Domain (**CD**), i.e., clean and adversarial image domains, also cooperate with HDF in learning disentangled features. The feature disentanglement is feasible because the adversarial capability is mainly entwined with the decision boundary of classifiers and is relatively independent of the intrinsic image signal, whereas a contrast holds true for the visual appearance. Here, we use two autoencoders with the same architecture but different weights to extract the features of clean images and their AEs separately, since many existing works [Stutz et al \(2019\)](#); [Lin et al \(2020\)](#) have pointed out

that regular AEs are off the manifold of clean images. It has also been verified that the Intrinsic Dimensionality (**ID**) of AEs is larger than that of clean images in [Qing et al \(2024\)](#), and data with higher ID are more difficult to be modeled by DNNs [Pope et al \(2020\)](#). Therefore, we reconstruct and disentangle clean images and AEs in CD for more precise feature representations.

After obtaining these well-trained autoencoders, in the attack stage against victim models, we iteratively optimize AFs of perturbed images using the natural evolution strategy [Wierstra et al \(2014\)](#), according to the query feedback from the victim model, while keeping the VF unaltered, until a successful AE is reconstructed from the fusion of the perturbed AF and the initial image’s VF. Here, the initial image refers to the starting point in the attack stage, which is usually set as the clean image in open-set scenarios or a transferable AE in close-set scenarios, depending on the applicability of surrogate models. More explanations about initial images will be clarified in the following sections. To the best of our knowledge, this is the first work that employs the hierarchical disentangled AFs and VFs in CD for black-box adversarial attacks. The contributions of our work can be summarized as follows:

- We design a new hierarchical disentanglement method to distill an AF, which has a significant impact on the image’s adversarial capability while minimizing its influence on visual perception, and a VF that has the opposite attributes, from an image’s latent feature;
- Based on this disentanglement, we propose a new query-efficient score-based black-box attack method, DifAttack++, which generates AEs by optimizing the AF according to the query feedback while maintaining the VF invariant;
- Experimental results demonstrate that DifAttack++ outperforms SOTA score-based black-box attack methods in ASR and query numbers simultaneously in almost all cases, meanwhile maintaining satisfactory visual quality of AEs, both for traditional and large-scale victim models.

Note that an earlier version of DifAttack++, called DifAttack, has been published in AAAI2024 [Liu et al \(2024b\)](#). Below, we summarize the differences of DifAttack++ from its conference version:

- DifAttack++ designs hierarchical convolution layers for the feature disentanglement, considering that one single layer of the Decouple-Fusion (**DF**) module in DifAttack is insufficient to disentangle intensely entangled AFs and VFs;
- Compared to DifAttack, in which clean images and their AEs share the same autoencoder for the image

reconstruction and feature disentanglement, the use of two cross-domain autoencoders in DifAttack++ achieves a more stable and faster training process, meanwhile leading to more effective black-box attack performance;

- DifAttack uses a clean image to start the attack stage in both close-set and open-set scenarios; but DifAttack++ adopts a transferable AE as the starting point in close-set scenarios for extracting more powerful AFs, resulting in better attack efficiency;
- The ASR and query efficiency of DifAttack++ far surpass those of DifAttack, e.g., average 17.2% higher ASR and 53.7% lower average query numbers, when performing targeted attacks on ImageNet against four complex victim models in closed-set scenarios.

The rest of this paper is organized as follows. Section 2 reviews related works on existing score-based black-box attack methods, together with the development of disentangled representation. Section 3 introduces the details of our DifAttack++ attack framework, including the training (Section 3.1) and attack (Section 3.2) stages. Section 4 shows the performance of DifAttack++ and comparisons with competing attack methods in terms of ASR, query efficiency, and visual quality. Finally, Section 5 gives a conclusion.

## 2 Related Works

### 2.1 Score-based Black-box Attack Methods

As our work mainly focuses on score-based black-box attack methods, we now conduct a literature review on such approaches.

Score-based black-box attack methods can be broadly categorized into three main classes: **transfer-based**, **query-based**, and **query-and-transfer-based** attacks [Feng et al \(2022\)](#). Transfer-based approaches query the black-box model once using AEs generated on local surrogate models, as explored in [Qin et al \(2023\)](#) and etc. These approaches take advantage of the transferability of AEs across classifiers with distinct architectures; but their ASRs generally are not satisfactory. The query-based techniques tackle the black-box optimization through iteratively querying the victim model. Some representatives are NES [Ilyas et al \(2018\)](#),  $\mathcal{N}$ Attack [Li et al \(2019\)](#), SimBA [Guo et al \(2019a\)](#), SignH [Al-Dujaili and O’Reilly \(2020\)](#), etc., which exhibit improved ASR performance compared to transfer-based approaches, albeit demanding a greater number of queries. Furthermore, the query-and-transfer-based methods amalgamate the merits of

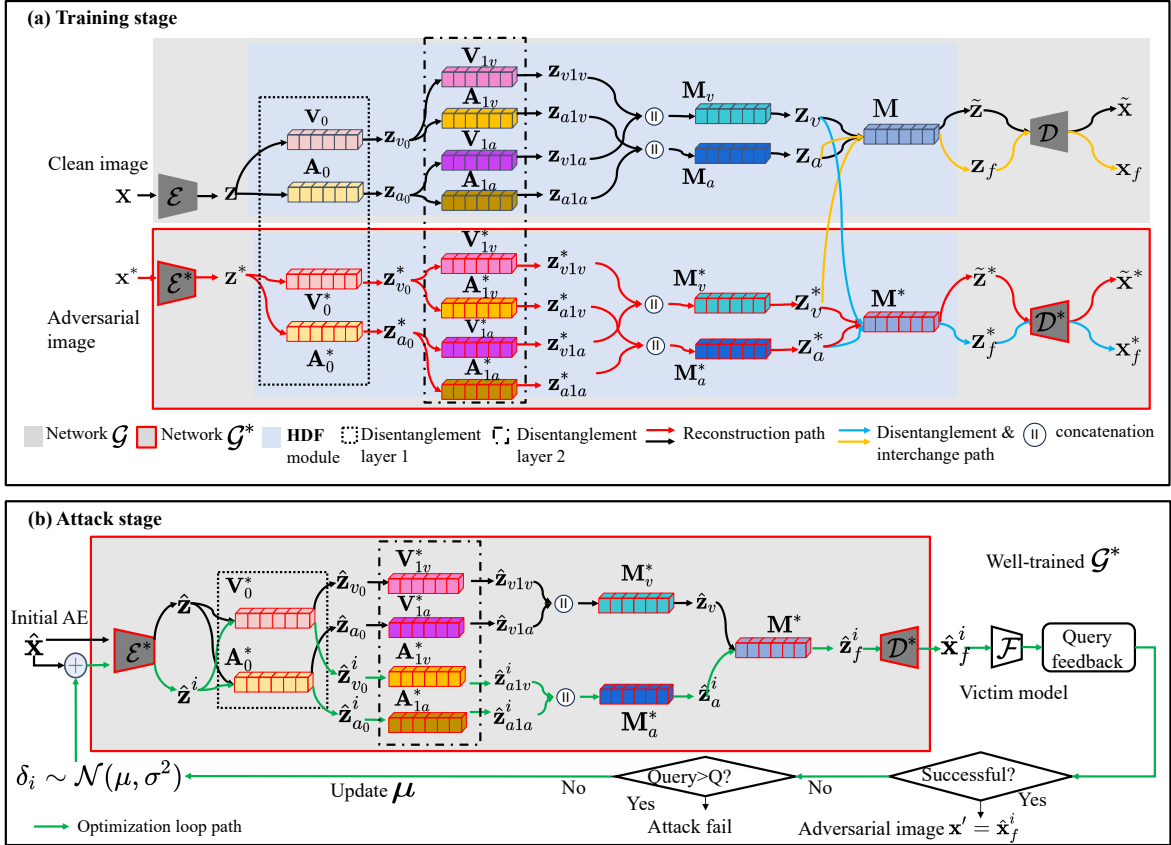


Fig. 1: (a) The training procedure of autoencoders  $\mathcal{G}$  and  $\mathcal{G}^*$  equipped with our proposed HDF module for disentangling adversarial and visual features. (b) The proposed black-box adversarial attack method, i.e. DifAttack++, incorporated with the pre-trained  $\mathcal{G}^*$ .

transfer-based and query-based techniques, resulting in an elevated ASR and smaller numbers of queries. For instance, Subspace Guo et al (2019b), P-RGF Cheng et al (2019), GFCS Lord et al (2022) and BASES Cai et al (2022) update queried AEs by performing white-box attacks against surrogate models with the guidance of the query feedback. There are some other methods that learn adversarial distributions by leveraging pairs of clean images and their AEs obtained by attacking surrogate models, e.g., TREMBA Huang and Zhang (2020) and CGA Feng et al (2022), or approximate the adversarial distribution with the clean data distribution, such as AdvFlow Mohaghegh Dolatabadi et al (2020). Then, the learned feature space for mapping the adversarial distribution is adopted as the search space of AEs. We also observe that some approaches incessantly refine auxiliary models using the query feedback to directly generate AEs Ma et al (2021), approximate decision boundaries Yin et al (2023) or gradients Du et al (2020) of victim models. However, these methods are often time-consuming and resource-intensive. Notably, MCG Yin et al (2023) achieves a remarkable ASR

and query efficiency by integrating SOTA query-based black-box methods with their proposed meta generator. This generator and surrogate models will be fine-tuned according to the query feedback for adapting to different victim models and test data distributions.

## 2.2 Disentangled Representation

As this work primarily focuses on attacking in the disentangled feature space, we also would like to briefly introduce the development of Disentangled Representation (DR), followed by a short review of adversarial attacks incorporating DR.

In Bengio et al (2013), it is intuitively defined that DR separates the distinct, independent and informative generative factors of variation in the data. Recently, many endeavors have embraced the utilization of autoencoders Lee et al (2020); Li et al (2023), generative adversarial networks Meo et al (2024), generative flows Ma et al (2020), and diffusion-based models Chen et al (2024); Yang et al (2024) to acquire dis-



entangled representations of data features, for which mutual information Burgess et al (2018); Kim et al (2021); Lin et al (2021) and total correlation Kim and Mnih (2018); Achille and Soatto (2018); Meo et al (2024) are mostly widely used. Regarding a more comprehensive discussion for DR, we refer interested readers to Wang et al (2022). DR has been broadly applied to the research on domain adaption Peng et al (2019); Cai et al (2019), image-to-image translation Gonzalez-Garcia et al (2018); Lee et al (2020), person re-identification Wei et al (2023), and pose estimation Nie and Liu (2021) etc.

As for the areas on adversarial attack and its defense strategies, DR has been commonly harnessed for detecting AEs or improving models’ robustness; see Mustafa et al (2020); Wang et al (2021); Yang et al (2021); Qing et al (2024). To the best of our knowledge, only a limited number of adversarial attack methods have involved DR, and all of them are *white-box* approaches. Along this line, RNF Kim et al (2021) optimizes image perturbations by maximizing the gradient of non-robust features in perturbed images, wherein non-robust features are distilled from the target classifier’s intermediate features. Another white-box attack method Lu et al (2021), called SSAE, trains an autoencoder to directly generate target models’ AEs. SSAE aims to minimize the norm difference of output logits between clean images and AEs to achieve better visual consistency, meanwhile maximizing the angle discrepancy of output logits for mis-classification.

Note that the disentanglement strategy of our DifAttack++ is quite different from the existing ones. White-box attack methods generally have prior knowledge of the victim model’s parameters and architecture during the DR learning, while DifAttack++ relies on surrogate models to learn DRs, with the particular challenging requirement of the generalizability of DRs across diverse classifiers. Furthermore, DifAttack++ disentangles image features capable of reconstructing the image signals, rather than the ones extracted by specific classifiers as Mustafa et al (2020); Kim et al (2021) do. Also, none of the existing methods disentangles adversarial capability and visual perception from latent features. As will be clear soon, the features disentangled by DifAttack++ are not closely related to specific categories or semantics, making DifAttack++ exhibit much more powerful disentanglement capability in open-set scenarios.

### 3 Proposed DifAttack++

Our DifAttack++ aims to use disentangled VFs and AFs of images to decode AEs in score-based black-box

settings, guided by the query feedback from the victim model. As illustrated in Fig. 1, DifAttack++ unfolds in two phases. In the training stage, we train two autoencoders  $\mathcal{G}$  and  $\mathcal{G}^*$  with the same model architecture but different weights. These two autoencoders both are able to conduct feature disentanglement and image reconstruction. The training images of  $\mathcal{G}$  and  $\mathcal{G}^*$  are a set of clean image  $\mathbf{x}$  and its AE  $\mathbf{x}^*$ , where  $\mathbf{x}^*$  is generated by performing an untargeted white-box attack on surrogate models. Taking  $\mathbf{x}$  as an example,  $\mathcal{G}$  can disentangle the latent feature  $\mathbf{z}$  of  $\mathbf{x}$  into the AF  $\mathbf{z}_a$  and VF  $\mathbf{z}_v$  via our proposed HDF module, and then reconstructs another image  $\tilde{\mathbf{x}}$  similar to  $\mathbf{x}$  by decoding the fusion of  $\mathbf{z}_a$  and  $\mathbf{z}_v$ . Likewise,  $\mathcal{G}^*$  also has the same functionality for its input.

In the attack stage, we leverage the pre-trained  $\mathcal{G}$  and  $\mathcal{G}^*$  to generate an AE  $\mathbf{x}'$  of  $\mathbf{x}$  against the black-box victim model  $\mathcal{F}$ . Specifically,  $\mathbf{x}'$  is obtained through an iterative optimization process, wherein we continuously sample a batch of perturbed images to extract their AFs  $\hat{\mathbf{z}}_a^i$ , while keeping the VF  $\hat{\mathbf{z}}_v$ , which is used for the subsequent image reconstruction along with  $\hat{\mathbf{z}}_a^i$ , consistent with that of the initial image. Such a process produces batches of reconstructed images  $\hat{\mathbf{x}}_f^i$  to query  $\mathcal{F}$ , until either the query number reaches its maximum threshold  $Q$ , or one of the perturbed images  $\hat{\mathbf{x}}_f^i$  successfully deceives  $\mathcal{F}$ , namely,  $\mathbf{x}' = \hat{\mathbf{x}}_f^i$ .

For clarity, a summary of notations frequently used in the following sections is provided in Table 1.

#### 3.1 Training Stage: Train Autoencoders $\mathcal{G}$ and $\mathcal{G}^*$

Let  $\mathbf{x}$  be a clean image in the training dataset  $\mathbb{T}$  and  $\mathbb{C}$  be the model set formed by the pre-trained white-box surrogate models based on  $\mathbb{T}$ . Note that these white-box surrogate models can be readily obtained and their availability has also been assumed in the existing approaches Lord et al (2022); Feng et al (2022). We adopt the white-box attack method PGD Madry et al (2018) to generate an AE  $\mathbf{x}^*$  of  $\mathbf{x}$ , by attacking a surrogate model  $\mathcal{C}_j$ . This  $\mathcal{C}_j$  is selected randomly from  $\mathbb{C}$ . Clearly, PGD can be replaced by other white-box attack methods or a collection of them (see the supplementary file of DifAttack Liu et al (2024b) for more details). Different from our previous work DifAttack which shares one autoencoder for both clean and adversarial images, in this work, we assign distinct autoencoders  $\mathcal{G}$  and  $\mathcal{G}^*$  for the clean and adversarial domains. Noticing that regular AEs usually lie off the manifold of normal images Lin et al (2020), the assignment of two autoencoders is more reasonable, and could lead to better training efficiency and black-box attack performance, as will be

Table 1: Notations

Signs	Descriptions
$\mathcal{F}$	Victim/target model
$\mathcal{G}$	Autoencoder trained on clean images
$\mathcal{G}^*$	Autoencoder trained on AEs
$\mathcal{E}$	Encoder in $\mathcal{G}$
$\mathcal{D}$	Decoder in $\mathcal{G}$
$\mathbf{V}_0$	1 <sup>st</sup> layer for extracting preliminary VFs
$\mathbf{A}_0$	1 <sup>st</sup> layer for extracting preliminary AFs
$\mathbf{V}_{1v}$	2 <sup>nd</sup> layer for extracting VFs from preliminary VFs
$\mathbf{V}_{1a}$	2 <sup>nd</sup> layer for extracting VFs from preliminary AFs
$\mathbf{A}_{1v}$	2 <sup>nd</sup> layer for extracting AFs from preliminary VFs
$\mathbf{A}_{1a}$	2 <sup>nd</sup> layer for extracting AFs from preliminary AFs
$\mathbf{M}_v$	Fusion layer for obtaining final VFs
$\mathbf{M}_a$	Fusion layer for obtaining final AFs
$\mathbf{M}$	Fusion layer for obtaining latent features
$\mathbf{x}$	$\mathbb{R}^d$ , Clean image
$\mathbf{x}^*$	$\mathbb{R}^d$ , AE of $\mathbf{x}$ crafted by white-box attacks
$\mathbf{x}'$	$\mathbb{R}^d$ , AE of $\mathbf{x}$ crafted by black-box attacks
$\tilde{\mathbf{x}}$	$\mathbb{R}^d$ , Reconstructed image of $\mathbf{x}$
$\hat{\mathbf{x}}$	$\mathbb{R}^d$ , Initial image in the attack stage
$\hat{\mathbf{x}}_f^i$	$\mathbb{R}^d$ , $i$ th reconstructed perturbed image
$\delta$	$\mathbb{R}^d$ , Image perturbation
$\mathbf{z}$	Latent features of $\mathbf{x}$
$\tilde{\mathbf{z}}$	Reconstructed latent features of $\mathbf{x}$
$\mathbf{z}_v$	Final VFs of $\mathbf{x}$
$\mathbf{z}_a$	Final AFs of $\mathbf{x}$
$\mathbf{z}_{v0}$	Preliminary VFs of $\mathbf{x}$
$\mathbf{z}_{a0}$	Preliminary AFs of $\mathbf{x}$
$\mathbf{z}_{v1v}$	VFs of $\mathbf{z}_{v0}$
$\mathbf{z}_{v1a}$	VFs of $\mathbf{z}_{a0}$
$\mathbf{z}_{a1v}$	AFs of $\mathbf{z}_{v0}$
$\mathbf{z}_{a1a}$	AFs of $\mathbf{z}_{a0}$
$\hat{\mathbf{z}}_a^i$	Final AFs of $i$ th perturbed image
$\hat{\mathbf{z}}_v$	Final VFs of image $\hat{\mathbf{x}}$
$\mathbf{z}_f$	Fused feature after feature interchange
$Q$	Maximum query number
$\mathbb{T}$	Training dataset
$\mathbb{C}$	Set of white-box surrogate models
$\mathcal{C}_j$	$j$ th white-box surrogate model in $\mathbb{C}$
$N$	Number of surrogate models in $\mathbb{C}$
$\mathcal{A}$	White-box attack method

<sup>1</sup> Other unmentioned symbols with \* mean that they are associated with AEs.

verified experimentally. Below, let us give the details on the disentanglement and reconstruction tasks.

### 3.1.1 Disentanglement.

For discovering an image’s AF to which the image’s adversarial capability is sensitive, meanwhile ensuring that alterations in this feature maintain minimal impact on the image’s visual appearance, we disentangle AFs and VFs from images’ latent feature. To this end, we exchange the AFs and VFs between a pair of clean image and its AE. Then two images reconstructed from these exchanged features are expected to exhibit different adversarial capabilities and visual appearance, according to the original images their features stem from.

**HDF Module.** Specifically, for implementing the feature disentanglement, as illustrated in Fig. 1(a), we design an HDF module, which accepts an image’s latent features as inputs and disentangles it into VFs and AFs. Eventually, HDF also generates this image’s reconstructed latent feature via fusing the VFs and AFs. HDF module consists of three kinds of convolution layers, including visual layers ( $\mathbf{V}_0$ ,  $\mathbf{V}_{1v}$  and  $\mathbf{V}_{1a}$ ), adversarial layers ( $\mathbf{A}_0$ ,  $\mathbf{A}_{1v}$  and  $\mathbf{A}_{1a}$ ), and fusion layers ( $\mathbf{M}_a$ ,  $\mathbf{M}_v$  and  $\mathbf{M}$ ), which are all implemented with a series of stacked  $1 \times 1$  convolution layers. Taking the clean image  $\mathbf{x}$  as an example, HDF feeds its latent feature  $\mathbf{z} = \mathcal{E}(\mathbf{x})$ , where  $\mathcal{E}$  denotes a Convolutional Neural Network (CNN)-based encoder, into the first disentanglement layer  $\mathbf{V}_0$  and  $\mathbf{A}_0$ , obtaining preliminary VFs  $\mathbf{z}_{v0}$  and AFs  $\mathbf{z}_{a0}$  respectively as:

$$\begin{aligned} \mathbf{z}_{v0} &= \mathbf{V}_0(\mathbf{z}), \\ \mathbf{z}_{a0} &= \mathbf{A}_0(\mathbf{z}). \end{aligned} \quad (1)$$

Considering that preliminary features  $\mathbf{z}_{v0}$  and  $\mathbf{z}_{a0}$  obtained from disentanglement layers at one level may still be coupled, we propose to hierarchically append the second disentanglement layers  $\mathbf{V}_{1v}$ ,  $\mathbf{V}_{1a}$ ,  $\mathbf{A}_{1v}$ , and  $\mathbf{A}_{1a}$  to preliminary features for achieving the finer disentanglement. These four layers are used for extracting the fine-grained VFs or AFs from preliminary VFs and AFs as follows:

$$\begin{aligned} \mathbf{z}_{v1v} &= \mathbf{V}_{1v}(\mathbf{z}_{v0}), \\ \mathbf{z}_{v1a} &= \mathbf{V}_{1a}(\mathbf{z}_{a0}), \\ \mathbf{z}_{a1v} &= \mathbf{A}_{1v}(\mathbf{z}_{v0}), \\ \mathbf{z}_{a1a} &= \mathbf{A}_{1a}(\mathbf{z}_{a0}). \end{aligned} \quad (2)$$

Then we adopt a visual fusion layer  $\mathbf{M}_v$  to combine these two hierarchically calibrated VFs  $\mathbf{z}_{v1v}$  and  $\mathbf{z}_{v1a}$ , leading to the final VFs  $\mathbf{z}_v$  of the input  $\mathbf{x}$ . Similarly, an adversarial fusion layer  $\mathbf{M}_a$  is employed to obtain the final AFs  $\mathbf{z}_a$  from  $\mathbf{z}_{a1v}$  and  $\mathbf{z}_{a1a}$ . Such a generation process can be formulated as:

$$\begin{aligned} \mathbf{z}_v &= \mathbf{M}_v(\mathbf{z}_{v1v} \parallel \mathbf{z}_{v1a}), \\ \mathbf{z}_a &= \mathbf{M}_a(\mathbf{z}_{a1v} \parallel \mathbf{z}_{a1a}), \end{aligned} \quad (3)$$

where  $\parallel$  denotes the channel-wise concatenation. Afterwards,  $\mathbf{z}_v$  and  $\mathbf{z}_a$  are incorporated into a reconstructed latent feature  $\tilde{\mathbf{z}}$  of  $\mathbf{z}$  via the fusion layer  $\mathbf{M}$ . Overall, we summarize the feature processing operations of the HDF module as:

$$\mathcal{HDF}(\mathbf{z}) = \mathbf{M}(\mathbf{z}_v \parallel \mathbf{z}_a) = \tilde{\mathbf{z}}. \quad (4)$$

For the clarity, we use  $\mathcal{HDF}(\cdot)$  and  $\mathcal{HDF}^*(\cdot)$  to represent HDF modules in networks  $\mathcal{G}$  and  $\mathcal{G}^*$ , respectively.

It is also easy to extend the process of  $\mathcal{HDF}^*(\cdot)$  with an input latent feature  $\mathbf{z}^*$  of an AE  $\mathbf{x}^*$  as:

$$\mathcal{HDF}^*(\mathbf{z}^*) = \mathbf{M}^*(\mathbf{z}_v^* || \mathbf{z}_a^*) = \tilde{\mathbf{z}}^*, \quad (5)$$

where  $\tilde{\mathbf{z}}^*$  denoted the reconstructed  $\mathbf{z}^*$  and  $\mathbf{M}^*$  is the fusion layer in  $\mathcal{G}^*$ . The final VFs  $\mathbf{z}_v^*$  and AFs  $\mathbf{z}_a^*$  of  $\mathbf{x}^*$  are obtained through the same process as in Eqs. (1)-(3), with the only difference being the substitution of modules of  $\mathcal{G}$  with modules of  $\mathcal{G}^*$ .

**Feature Interchange in CD.** After elucidating the HDF module, we now introduce how to utilize HDF to conduct the feature interchange in CD for accomplishing the disentanglement. Specifically, as depicted by the yellow path in Fig. 1(a), the AF of the clean sample (clean domain), i.e.  $\mathbf{z}_a$ , is firstly concatenated with the VF of the adversarial image (adversarial domain), i.e.  $\mathbf{z}_v^*$ . Afterwards, they are fed into the fusion layer  $\mathbf{M}$  to obtain the fused feature  $\mathbf{z}_f$ . Symmetrically, as shown by the blue path, we can obtain another fused feature  $\mathbf{z}_f^*$ . These two steps can be expressed as:

$$\begin{aligned} \mathbf{z}_f &= \mathbf{M}(\mathbf{z}_v^* || \mathbf{z}_a), \\ \mathbf{z}_f^* &= \mathbf{M}^*(\mathbf{z}_v || \mathbf{z}_a^*). \end{aligned} \quad (6)$$

With these two features in hand, we can naturally reconstruct images  $\mathbf{x}_f$  and  $\mathbf{x}_f^*$  by:

$$\begin{aligned} \mathbf{x}_f &= \mathcal{D}(\mathbf{z}_f), \\ \mathbf{x}_f^* &= \mathcal{D}^*(\mathbf{z}_f^*). \end{aligned} \quad (7)$$

where  $\mathcal{D}$  and  $\mathcal{D}^*$  denote the CNN-based decoder in  $\mathcal{G}$  and  $\mathcal{G}^*$ , respectively.

**Disentanglement Loss.** Subsequently, since we desire the AF to control the adversarial capability of the image, while the VF to govern its visual perception,  $\mathbf{x}_f$  should be closer to the visual perception of the AE  $\mathbf{x}^*$  and be non-adversarial. Conversely,  $\mathbf{x}_f^*$  is expected to be closer to the visual perception of the clean image  $\mathbf{x}$ , and be adversarial against all surrogate models so as to improve the generalization ability of the AF on different classifiers. Hence, we aim to minimize the disentanglement loss  $L_{dis}$  that is defined as:

$$\begin{aligned} L_{dis} &= \|\mathbf{x}^* - \mathbf{x}_f\|_2 + \frac{1}{N} \sum_{j=1}^N L_{adv}(\mathbf{x}_f, y, 1, \mathcal{C}_j, k) \\ &+ \|\mathbf{x} - \mathbf{x}_f^*\|_2 + \frac{1}{N} \sum_{j=1}^N L_{adv}(\mathbf{x}_f^*, y, 0, \mathcal{C}_j, k), \end{aligned} \quad (8)$$

where  $N$  signifies the cardinality of the surrogate model set  $\mathcal{C}$ . The  $l_2$  norm measures the Euclidean distance of two images, and  $L_{adv}$  is employed to evaluate the adversarial ability, whose definition [Carlini and Wagner \(2017\)](#) is:

$$\begin{aligned} L_{adv}(\mathbf{x}, y, v, \mathcal{C}_j, k) &= \\ \max \left\{ \mathbb{I}(v) \cdot (\mathcal{C}_j(\mathbf{x}, y) - \max_{h \neq y} \mathcal{C}_j(\mathbf{x}, h)), -k \right\}. \end{aligned} \quad (9)$$

Here, the value of  $v$  can be set as 0 or 1.  $\mathbb{I}(0) = 1$  means an untargeted attack with a ground-truth label of  $y$ , while  $\mathbb{I}(1) = -1$  indicates a targeted attack with a target category of  $y$ . Also,  $\mathcal{C}_j(\mathbf{x}, h)$  is the output score of  $\mathcal{C}_j$  for the  $h$ -th class. The adjustable constant  $k > 0$  controls the adversarial extent.

### 3.1.2 Reconstruction.

For achieving a cycle consistency [Zhu et al \(2017\)](#) with regard to the feature disentanglement, as depicted in the reconstruction paths of Fig. 1(a), the autoencoder is expected to reconstruct an input image well even when its latent feature is processed by the HDF module. Therefore, the output of HDF modules, i.e.  $\tilde{\mathbf{z}}$  and  $\tilde{\mathbf{z}}^*$ , are expected to reconstruct two images  $\tilde{\mathbf{x}} \approx \mathbf{x}$  and  $\tilde{\mathbf{x}}^* \approx \mathbf{x}^*$  through:

$$\begin{aligned} \tilde{\mathbf{x}} &= \mathcal{D}(\mathcal{HDF}(\mathbf{z})), \\ \tilde{\mathbf{x}}^* &= \mathcal{D}^*(\mathcal{HDF}^*(\mathbf{z}^*)). \end{aligned} \quad (10)$$

Consequently, we define the reconstruction loss  $L_{rec}$  of  $\mathcal{G}$  and  $\mathcal{G}^*$  by:

$$L_{rec} = \|\mathbf{x} - \tilde{\mathbf{x}}\|_2 + \|\mathbf{x}^* - \tilde{\mathbf{x}}^*\|_2. \quad (11)$$

Eventually, the loss function to be minimized during training networks  $\mathcal{G}$  and  $\mathcal{G}^*$  can be computed as:

$$L_{all} = \lambda \cdot L_{rec} + L_{dis}, \quad (12)$$

where the hyper-parameter  $\lambda$  balances two loss terms.

### 3.2 Attack Stage: Generate the AE $\mathbf{x}'$

Upon obtaining the well-trained  $\mathcal{G}$  and  $\mathcal{G}^*$ , in the subsequent attack stage, we utilize them to generate AEs in a black-box setting. As shown in Fig. 1(b), to perform a black-box attack against the victim model  $\mathcal{F}$  with a clean image  $\mathbf{x}$ , we maintain the VF for decoding the perturbed image  $\hat{\mathbf{x}}_f^i$  to be identical to that of the initial image  $\hat{\mathbf{x}}$ , i.e.  $\hat{\mathbf{z}}_v$  that is obtained by:

$$\begin{aligned} \hat{\mathbf{z}} &= \mathcal{E}^*(\hat{\mathbf{x}}), \\ \hat{\mathbf{z}}_{v0} &= \mathbf{V}_0^*(\hat{\mathbf{z}}), \\ \hat{\mathbf{z}}_{a0} &= \mathbf{A}_0^*(\hat{\mathbf{z}}), \\ \hat{\mathbf{z}}_{v1v} &= \mathbf{V}_{1v}^*(\hat{\mathbf{z}}_{v0}), \\ \hat{\mathbf{z}}_{v1a} &= \mathbf{V}_{1a}^*(\hat{\mathbf{z}}_{a0}), \\ \hat{\mathbf{z}}_v &= \mathbf{M}_v^*(\hat{\mathbf{z}}_{v1v} || \hat{\mathbf{z}}_{v1a}). \end{aligned} \quad (13)$$

This makes  $\hat{\mathbf{x}}_f^i$  remain in close proximity to the clean image as much as possible. Meanwhile, our another objective is to identify an AF  $\hat{\mathbf{z}}_a^i$  that, when combined with  $\hat{\mathbf{z}}_v$ , has the ability to deceive the victim model  $\mathcal{F}$ .

**Algorithm 1** The proposed DifAttack++.

**Input:** Target classifier  $\mathcal{F}$ ; autoencoder  $\mathcal{G}^*$  pretrained in the adversarial domain; clean image  $\mathbf{x}$ ; initial image  $\hat{\mathbf{x}}$ ; max query budget  $Q$ ; distortion budget  $\epsilon$ ; ground-truth/target label  $y$  for untargeted/targeted attacks; learning rate  $\eta$ ; variance  $\sigma$ ;  $v, k$  in Eq.(18); sample scale  $\tau$ .

**Output:** Adversarial image  $\mathbf{x}'$ .

```

1: Let  $q \leftarrow 0, \mathbf{x}' \leftarrow \hat{\mathbf{x}}, \mu \sim \mathcal{N}(0, I)$ 
2: while  $q + \tau \leq Q$  do
3:    $\gamma_1, \dots, \gamma_i, \dots, \gamma_\tau \sim \mathcal{N}(0, I)$ 
4:    $\delta_i \leftarrow \mu + \sigma\gamma_i, \forall i \in \{1, \dots, \tau\}$ 
5:   if In close-set scenarios then
6:     Obtaining  $\hat{\mathbf{x}}_f^i$  using Eqs. (15), (13), (16), and (17).
7:   else if In open-set scenarios then
8:     Obtaining  $\hat{\mathbf{x}}_f^i$  using Eqs. (21), (22), (16), and (17).
9:   end if
10:   $l_i \leftarrow L_{adv}(\hat{\mathbf{x}}_f^i, y, v, \mathcal{F}, k), \forall i$ 
11:   $q \leftarrow q + \tau$ 
12:  if  $\exists l_i = -k$  then
13:     $\mathbf{x}' \leftarrow \hat{\mathbf{x}}_f^i$ 
14:    break
15:  else
16:     $\hat{l}_i \leftarrow (l_i - \text{mean}(\{l_i\})) / \text{std}(\{l_i\}), \forall i$ 
17:     $\mu \leftarrow \mu - \frac{\eta}{\tau\sigma} \sum_{i=1}^{\tau} \hat{l}_i \gamma_i$ 
18:  end if
19: end while
20: return  $\mathbf{x}'$ 

```

For example, in untargeted attacks, our attack objective targets at finding an image  $\hat{\mathbf{x}}_f^i$  by:

$$\hat{\mathbf{x}}_f^i = \mathcal{D}^*(\mathbf{M}^*(\hat{\mathbf{z}}_v || \hat{\mathbf{z}}_a^i)),$$

$$s.t. \arg \max_{\mathbf{h}} \mathcal{F}(\hat{\mathbf{x}}_f^i, h) \neq y \text{ and } \|\hat{\mathbf{x}}_f^i - \mathbf{x}\|_p \leq \epsilon. \quad (14)$$

Here  $y$  denotes the ground-truth label of  $\mathbf{x}$ . In targeted attacks, the first constraint is transformed to  $\arg \max_{\mathbf{h}} \mathcal{F}(\hat{\mathbf{x}}_f^i, h) = y$  with  $y$  being the target class. Note that in Eqs. (13) and (14) we use modules of  $\mathcal{G}^*$  rather than  $\mathcal{G}$ , and the reason will be clarified later.

For seeking out such a  $\hat{\mathbf{z}}_a^i$  to meet Eq. (14), we first have to determine the initial image  $\hat{\mathbf{x}}$  for the attack stage so as to acquire  $\hat{\mathbf{z}}_v$ ; similar to Eq. (13). Considering the adversarial transferability across different models, we leverage an AE rather than the clean image to initialize a more aggressive AF, expecting to enhance the attack efficiency. This initialization strategy is feasible with known class information and available surrogate models in closed-set scenarios, since we can directly generate a transferable AE through a white-box attack method against surrogate models. However, in open-set scenarios, due to the uncertainty of class categories, a clean image would be more suitable for initializing the attack, i.e.  $\hat{\mathbf{x}} = \mathbf{x}$ . Below, we elaborate on the attack processes separately for the closed-set and open-set scenarios.

### 3.2.1 Close-set scenarios

In closed-set scenarios, as illustrated in Fig. 1(b), we first generate a transferable AE  $\hat{\mathbf{x}}$  of  $\mathbf{x}$  against an ensemble of local surrogate models using a transferable white-box attack method  $\mathcal{A}$ . In this work, we choose SI-NI-TI-DIM Lin et al (2019) as  $\mathcal{A}$ , which is currently one of the most effective transferable white-box attack methods. Of course,  $\mathcal{A}$  could be replaced by other potentially stronger methods that may emerge in the future. Formally, the generation of the initial image at the untargeted attack stage is expressed as:

$$\hat{\mathbf{x}} = \mathcal{A}(\mathbb{C}, \mathbf{x}),$$

$$s.t. \arg \max_{\mathbf{h}} \mathcal{C}_j(\hat{\mathbf{x}}, h) \neq y \text{ and } \|\hat{\mathbf{x}} - \mathbf{x}\|_p \leq \epsilon, \forall \mathcal{C}_j \in \mathbb{C}. \quad (15)$$

For targeted black-box attacks, this formulation only needs to replace the constraint  $\arg \max_{\mathbf{h}} \mathcal{C}_j(\hat{\mathbf{x}}, h) \neq y$  where  $y$  represents the ground-truth label with  $\arg \max_{\mathbf{h}} \mathcal{C}_j(\hat{\mathbf{x}}, h) = y$  where  $y$  denotes the target label. Then we can combine Eqs. (15) and (13) to produce  $\hat{\mathbf{z}}_v$ , and maintain the VF for decoding the perturbed candidate image  $\hat{\mathbf{x}}_f^i$  to be identical to the VF of  $\hat{\mathbf{x}}$ , i.e.  $\hat{\mathbf{z}}_v$ . Note that  $\hat{\mathbf{z}}_v$  in Eq. (13) is disentangled by  $\mathcal{G}^*$  but not  $\mathcal{G}$  since  $\hat{\mathbf{x}}$  belongs to the adversarial domain. Then, we also need to identify proper AFs  $\hat{\mathbf{z}}_a^i$  that, when fused with  $\hat{\mathbf{z}}_v$ , has the ability to deceive  $\mathcal{F}$ . Therefore, we aim to discover a perturbation  $\delta_i$  whose corresponding perturbed image  $\hat{\mathbf{x}} + \delta_i$  can be used to extract such AFs. Formally, we obtain  $\hat{\mathbf{z}}_a^i$  via:

$$\hat{\mathbf{z}}^i = \mathcal{E}^*(\hat{\mathbf{x}} + \delta_i),$$

$$\hat{\mathbf{z}}_{v0}^i = \mathbf{V}_0^*(\hat{\mathbf{z}}^i),$$

$$\hat{\mathbf{z}}_{a0}^i = \mathbf{A}_0^*(\hat{\mathbf{z}}^i),$$

$$\hat{\mathbf{z}}_{a1v}^i = \mathbf{A}_{1v}^*(\hat{\mathbf{z}}_{v0}^i),$$

$$\hat{\mathbf{z}}_{a1a}^i = \mathbf{A}_{1a}^*(\hat{\mathbf{z}}_{a0}^i),$$

$$\hat{\mathbf{z}}_a^i = \mathbf{M}_a^*(\hat{\mathbf{z}}_{a1v}^i || \hat{\mathbf{z}}_{a1a}^i). \quad (16)$$

Then in close-set scenarios, the perturbed AE  $\hat{\mathbf{x}}_f^i$  can be reconstructed as follows:

$$\hat{\mathbf{x}}_f^i = \Pi_{\epsilon, \mathbf{x}} \left( \mathcal{D}^* \left( \mathbf{M}^*(\hat{\mathbf{z}}_v || \hat{\mathbf{z}}_a^i) \right) \right). \quad (17)$$

where  $\hat{\mathbf{z}}_v$  is obtained by Eq. (13) and keeps invariant while  $\hat{\mathbf{z}}_a^i$  is iteratively optimized by using Eq. (16) and continuously updated  $\delta_i$ . Here, the operation  $\Pi_{\epsilon, \mathbf{x}}$  represents the projection of the input image onto the  $l_p$  ball bounded by  $\epsilon$  and centered at  $\mathbf{x}$ . This forces the adversarial perturbation to remain within the specified constraint. For simplicity, we recast the right-hand side of Eq.(17) as  $\mathbf{T}(\hat{\mathbf{x}} + \delta_i)$ . To find an adversarial  $\hat{\mathbf{x}}_f^i$ , by



combining Eq.(17) and using the transformation of variable approach, we formulate our attack objective in Eq. (14) in a unified manner as:

$$\begin{aligned} \min_{\mu} \mathbb{E}_{\mathcal{N}(\delta_i|\mu,\sigma^2)} L_{adv}(\mathbf{T}(\hat{\mathbf{x}} + \delta_i), y, v, \mathcal{F}, k), \\ \text{s.t. } \|\mathbf{T}(\hat{\mathbf{x}} + \delta_i) - \mathbf{x}\| \leq \epsilon, \end{aligned} \quad (18)$$

where  $\hat{\mathbf{x}}_f^i = \mathbf{T}(\hat{\mathbf{x}} + \delta_i)$  satisfies  $\arg \max_h \mathcal{F}(\hat{\mathbf{x}}_f^i, h) \neq y$  for untargeted attacks with  $y$  representing the ground-truth label of  $\mathbf{x}$  or  $\arg \max_h \mathcal{F}(\hat{\mathbf{x}}_f^i, h) = y$  for targeted attacks with  $y$  denoting the target class. We sample  $\delta_i$  from a Gaussian distribution  $\mathcal{N}(\mu, \sigma^2)$  where the mean  $\mu$  is to be optimized and the variance  $\sigma$  is fixed to be the optimal value through performing a grid search. For optimizing  $\mu$ , we adopt the natural evolution strategies method to estimate the gradient of the expectation of  $L_{adv}$  in Eq.(18) with respect to  $\mu$ . When using stochastic gradient descent with a learning rate  $\eta$  and a batch size  $\tau$ , the updating rule for  $\mu$  is as follows:

$$\mu \leftarrow \mu - \frac{\eta}{\tau\sigma} \sum_{i=1}^{\tau} \gamma_i L_{adv}(\mathbf{T}(\hat{\mathbf{x}} + \mu + \sigma\gamma_i), y, v, \mathcal{F}, k). \quad (19)$$

where  $\gamma_i \sim \mathcal{N}(0, I)$ , and by setting  $\delta_i = \mu + \sigma\gamma_i$ , we obtain  $\delta_i \sim \mathcal{N}(\mu, \sigma^2)$ . When we obtain a feasible solution for  $\mu$  in Eq. (18) using Eq. (19), we are able to sample at least one successful AE  $\mathbf{x}'$  by calculating:

$$\mathbf{x}' = \hat{\mathbf{x}}_f^i = \mathbf{T}(\hat{\mathbf{x}} + \mu + \sigma\gamma_i). \quad (20)$$

### 3.2.2 Open-set scenarios

In open-set scenarios, due to the uncertainty of images' categories, surrogate models are highly likely to predict outputs inconsistent with that of victim models and consequently generate AEs with rather weak transferabilities. In these scenarios, we hence set the clean image  $\mathbf{x}$  as the initial image  $\hat{\mathbf{x}}$ , i.e.

$$\hat{\mathbf{x}} = \mathbf{x}, \quad (21)$$

and disentangle VFs of  $\hat{\mathbf{x}}$  via  $\mathcal{G}$  that belongs to the clean domain as:

$$\begin{aligned} \hat{\mathbf{z}} &= \mathcal{E}(\hat{\mathbf{x}}), \\ \hat{\mathbf{z}}_{v0} &= \mathbf{V}_0(\hat{\mathbf{z}}), \\ \hat{\mathbf{z}}_{a0} &= \mathbf{A}_0(\hat{\mathbf{z}}), \\ \hat{\mathbf{z}}_{v1v} &= \mathbf{V}_{1v}(\hat{\mathbf{z}}_{v0}), \\ \hat{\mathbf{z}}_{v1a} &= \mathbf{V}_{1a}(\hat{\mathbf{z}}_{a0}), \\ \hat{\mathbf{z}}_v &= \mathbf{M}_v(\hat{\mathbf{z}}_{v1v} \parallel \hat{\mathbf{z}}_{v1a}). \end{aligned} \quad (22)$$

Meanwhile, we still extract AFs  $\hat{\mathbf{z}}_a^i$  of the perturbed image  $\hat{\mathbf{x}} + \delta_i$  with  $\mathcal{G}^*$  as Eq. (16) to keep fused  $\hat{\mathbf{x}}_f^i$  lie on the adversarial domain as much as possible. Similar

to close-set scenarios, it is easy to obtain the perturbed image  $\hat{\mathbf{x}}_f^i$  in open-set scenarios as in Eq. (17); but obtaining  $\hat{\mathbf{z}}_v$  in Eq. (17) using Eqs. (21) and (22) sequentially, and acquiring  $\hat{\mathbf{z}}_a^i$  by Eq. (16). Then we can use the same solution as in the closed-set scenarios mentioned above to obtain a successful AE  $\mathbf{x}'$ .

Overall, our DifAttack++ is summarized in Algorithm 1. Note that, in line 16, we normalize the  $L_{adv}$  of each perturbed image to stabilize convergence by taking inspiration from the  $\mathcal{N}$ Attack Li et al (2019) method.

## 4 Experiments

In this section, we compare our DifAttack++ with SOTA score-based black-box attack methods in both close-set and open-set scenarios. Ablation studies on the number of disentanglement layers, the CD, the HDF module, and the selected initial image in the attack stage will also be conducted.

### 4.1 Experiment Setup

#### 4.1.1 Datasets.

We mainly perform experiments on the large-scale ImageNet-1k (abbreviated as ImageNet) Deng et al (2009) dataset in close-set scenarios, on Food101 Bossard et al (2014) and ObjectNet Barbu et al (2019) in open-set scenarios. Specifically, Food101 consists of 101 food categories, and ObjectNet contains natural images with controls for rotation, background, and viewpoint, which poses challenges for object recognition. As a common practice, images in ImageNet, Food101 and ObjectNet are cropped and resized to  $224 \times 224$ ,  $224 \times 224$  and  $336 \times 336$  for adapting their associated classifiers. When conducting attacks on ObjectNet in open-set scenarios, we exclude 131 classes that overlap with ImageNet. More details about these classes can be found in Barbu et al (2019).

#### 4.1.2 Classifiers.

For ImageNet, we collect eight pre-trained classifiers with different architectures, i.e. ResNet18, VGG16, GoogleNet, SqueezeNet, ConvNeXtBase, EfficientNet-B3, Swin-V2-T, and ResNet101 provided by torchvision<sup>2</sup>. Their top-1 classification accuracies on the ImageNet validation dataset are 69.8%, 73.4%, 69.8%, 58.2%, 84.1%, 82.0%, 82.1%, and 81.9% respectively. These eight classifiers are divided into two groups for

<sup>2</sup> <https://pytorch.org/vision/stable/index.html>

Table 2: Results of score-based black-box attacks on ImageNet for the “*simple group*”. Attack success rate (ASR %) and average number of queries (Avg.Q) are used as metrics. For target attacks, the class 864 is selected as the target. The best and second best ASR and Avg.Q results are **bold** and underlined, respectively.

Victims	GoogleNet				VGG16				ResNet18				SqueezeNet				Average			
	Targeted		Untargeted		Targeted		Untargeted		Targeted		Untargeted		Targeted		Untargeted		Targeted		Untargeted	
Metrics	ASR	Avg.Q	ASR	Avg.Q	ASR	Avg.Q	ASR	Avg.Q	ASR	Avg.Q	ASR	Avg.Q	ASR	Avg.Q	ASR	Avg.Q	ASR	Avg.Q	ASR	Avg.Q
SignH	28.1%	9,021	95.5%	1,504	60.8%	7,606	<b>100.0%</b>	702	49.8%	7,935	<u>99.5%</u>	931	45.7%	8,315	<b>100.0%</b>	363	46.1%	8,219	98.8%	875
NES	37.7%	8,748	<b>100.0%</b>	1,234	47.7%	8,328	98.0%	1,068	54.3%	7,988	97.5%	1,264	45.7%	8,235	91.0%	1,711	46.4%	8,325	96.6%	1,319
$\mathcal{N}$ Attack	76.9%	6,883	<b>100.0%</b>	878	93.5%	5,924	<b>100.0%</b>	752	94.5%	5,324	<b>100.0%</b>	780	90.0%	5,644	<b>100.0%</b>	563	88.7%	5,944	<b>100.0%</b>	743
SimBA	77.5%	5,874	<b>100.0%</b>	865	<u>97.5%</u>	3,505	99.0%	533	97.0%	3,873	<u>99.5%</u>	614	94.0%	4,230	<u>99.5%</u>	428	91.5%	4,371	<u>99.5%</u>	610
BASES	12.5%	8,901	81.7%	2,080	26.7%	8,229	95.5%	564	15.4%	9,228	<u>85.1%</u>	1,717	35.3%	7,179	86.4%	1,549	22.5%	8,384	<u>87.2%</u>	1,478
P-RGF	34.2%	7,790	93.0%	1,162	58.3%	6,093	98.0%	529	51.3%	6,393	96.0%	711	65.3%	5,433	95.0%	796	52.3%	6,427	95.5%	800
Subspace	50.3%	6,642	95.5%	994	68.3%	4,964	<u>95.5%</u>	867	66.3%	4,750	94.5%	917	33.2%	8,063	97.0%	566	54.5%	6,105	95.6%	836
GFCS	60.0%	6,359	<u>96.5%</u>	1,348	93.0%	3,358	<b>100.0%</b>	515	95.0%	3,274	<b>100.0%</b>	739	72.5%	6,127	98.5%	658	80.1%	4,780	98.8%	815
CGA	90.9%	4,645	<b>100.0%</b>	<u>139</u>	91.1%	4,801	<u>99.4%</u>	137	91.6%	4,222	97.3%	475	93.2%	3,972	99.3%	202	91.7%	4,410	99.0%	238
MCGSquare	96.0%	2,937	<b>100.0%</b>	174	<b>100.0%</b>	<u>1,816</u>	<b>100.0%</b>	49	<u>99.5%</u>	<u>1,346</u>	<b>100.0%</b>	<b>61</b>	<b>99.0%</b>	<u>1,633</u>	<b>100.0%</b>	<b>37</b>	98.6%	<u>1,933</u>	<b>100.0%</b>	<u>180</u>
DifAttack	<u>97.0%</u>	3,201	<b>100.0%</b>	165	<b>100.0%</b>	2,246	<b>100.0%</b>	123	<b>100.0%</b>	1,901	<b>100.0%</b>	156	98.0%	2,793	<b>100.0%</b>	<b>90</b>	<u>98.8%</u>	2,535	<b>100.0%</b>	134
DifAttack++	<b>99.5%</b>	<b>1,530</b>	<b>100.0%</b>	<b>80</b>	<b>100.0%</b>	<b>969</b>	<b>100.0%</b>	<b>52</b>	<b>100.0%</b>	<b>957</b>	<b>100.0%</b>	<b>62</b>	<b>99.0%</b>	<b>1,389</b>	<b>100.0%</b>	<b>41</b>	<b>99.6%</b>	<b>1,211</b>	<b>100.0%</b>	<b>58</b>

Table 3: Results of score-based black-box attacks on ImageNet for the “*complex group*”. Attack success rate (ASR %) and average number of queries (Avg.Q) are used as metrics. For target attacks, the class 864 is selected as the target. The best and second best ASR and Avg.Q results are **bold** and underlined, respectively.

Victims	Swin-V2-T				EfficientNet-B3				ResNet101				ConvNeXtBase				Avg.			
	Targeted		Untargeted		Targeted		Untargeted		Targeted		Untargeted		Targeted		Untargeted		Targeted		Untargeted	
Metrics	ASR	Avg.Q	ASR	Avg.Q	ASR	Avg.Q	ASR	Avg.Q	ASR	Avg.Q	ASR	Avg.Q	ASR	Avg.Q	ASR	Avg.Q	ASR	Avg.Q	ASR	Avg.Q
SignH	44.2%	8,212	82.9%	3,049	31.7%	8,847	87.4%	2,611	6.5%	9,744	66.3%	4,670	20.6%	9,216	81.9%	3,979	25.8%	9,005	79.6%	3,577
NES	30.7%	8,722	95.0%	2,093	15.6%	9,382	95.5%	2,185	10.6%	9,606	90.0%	3,013	11.1%	9,471	86.4%	3,561	17.0%	9,295	91.7%	2,713
NAttack	66.8%	7,473	99.0%	1,298	32.2%	8,825	99.0%	1,390	20.6%	9,128	96.5%	1,888	40.7%	8,609	<b>100.0%</b>	2,012	40.1%	8,509	98.6%	1,647
SimBA	84.0%	5,822	98.5%	2,185	65.0%	7,585	98.0%	1,419	30.5%	9,579	73.0%	5,314	90.0%	5,328	98.5%	1,885	67.4%	7,078	92.0%	2,701
P-RGF	62.3%	4,610	96.5%	755	49.3%	6,244	90.0%	1,345	34.7%	8,087	89.5%	1,301	57.3%	5,720	88.9%	1,381	50.9%	6,165	91.2%	1,196
Subspace	61.3%	6,597	99.0%	882	55.3%	6,834	95.5%	993	35.7%	7,978	95.5%	1,198	76.9%	5,206	99.0%	569	57.3%	6,654	97.2%	910
GFCS	61.5%	5,683	86.5%	1,794	57.0%	5,897	89.0%	1,692	36.0%	7,577	87.0%	1,521	71.0%	4,270	91.5%	1,621	56.4%	5,857	88.5%	1,657
MCGSquare	99.0%	2,352	<b>100.0%</b>	<u>251</u>	<b>95.0%</b>	3,738	<u>99.5%</u>	463	<u>75.5%</u>	6,079	<b>99.5%</b>	400	<b>100.0%</b>	2,762	<b>100.0%</b>	226	<u>92.4%</u>	3,733	<u>99.8%</u>	<u>335</u>
DifAttack	95.0%	3,962	<b>100.0%</b>	454	62.0%	6,555	<b>100.0%</b>	605	50.0%	7,466	99.0%	675	98.0%	4,625	<b>100.0%</b>	662	76.3%	5,652	<u>99.8%</u>	599
DifAttack++	<b>100.0%</b>	<b>986</b>	<b>100.0%</b>	<b>137</b>	<u>92.0%</u>	<b>3,711</b>	<b>100.0%</b>	<b>225</b>	<b>82.0%</b>	<b>4,285</b>	<b>99.5%</b>	<b>264</b>	<b>100.0%</b>	<b>1,495</b>	<b>100.0%</b>	<b>159</b>	<b>93.5%</b>	<b>2,619</b>	<b>99.9%</b>	<b>196</b>

experiments. The first group, referred to as the “simple group”, consists of the former four classifiers with relatively lower classification accuracy (below 80%) and simple architectures, which have also been used in DifAttack. The second group, denoted as the “complex group”, comprises the remaining four classifiers, which have not been investigated in DifAttack. These models exhibit higher accuracy (above 80%), with more diverse and advanced architectures. We select three classifiers from each group to compose the set of surrogate models, while the remaining one in the same group serves as the victim model. In addition, for Food101 and ObjectNet, we use well pretrained OpenAI’s CLIP models provided by Ilharco et al (2021) as victim models to further verify the attack ability of DifAttack++ towards foundation models. These two models are ViT-B/16 trained on publicly available image-caption data and ViT-H-14-CLIPA-336 trained on DataComp-1B dataset Gadre et al (2024), achieving 88.7% and 77.4% zero-shot accuracy on Food101 and ObjectNet, respectively.

#### 4.1.3 Comparative Methods.

We compare our DifAttack++ with SOTA score-based black-box attack approaches, including DifAttack Liu et al (2024b), MCG Yin et al (2023), CGA Feng et al

(2022), GFCS Lord et al (2022), BASES Cai et al (2022), SignH Al-Dujaili and O’Reilly (2020), SimBA-DCT (shorted as SimBA) Guo et al (2019a),  $\mathcal{N}$ Attack Li et al (2019), P-RGF Cheng et al (2019), Subspace Guo et al (2019b), and NES Ilyas et al (2018). We evaluate them according to their official source codes. Due to the absence of pre-trained models and code, the experimental results of the CGA on ImageNet are directly copied from Feng et al (2022). Since MCG Yin et al (2023) could improve the query efficiency of the black-box attack method being combined with, meanwhile SquareAttack is at the top of the Black-boxBench leaderboard Zheng et al (2023, 2024), we choose the best query-efficient combination (see also Yin et al (2023)), MCG+SquareAttack Andriushchenko et al (2020) dubbed as MCGSquare as a representative method to compare with.

#### 4.1.4 Parameters.

Following many previous works, we set the maximum perturbation on ImageNet, Food101 and ObjectNet to 12/255, and the maximum query number to 10,000. For the real-world Imagga API, the maximum query number is limited to 500 due to the practical constraints.



Fig. 2: The visualization of AEs produced by MCGSquare [Andriushchenko et al \(2020\)](#) and DifAttack++.

Table 4: The visual quality comparison of AEs on ImageNet. AEs are generated by DifAttack++ or MCGSquare.

Methods	PSNR $\uparrow$	SSIM $\uparrow$	LPIPS $\downarrow$	MSE $\downarrow$
MCGSquare	24.96	0.7109	0.3154	27.26
<b>DifAttack++</b>	<b>27.51</b>	<b>0.7844</b>	<b>0.2010</b>	<b>22.36</b>

Also, in our DifAttack++, we set  $\lambda = 1$ ,  $\sigma = 0.1$ ,  $\eta = 0.01$ ,  $k = 5$  or  $0$  in Eqs.(8) and (19).

#### 4.2 The Close-set Scenario

Tables 2 and 3 present the results on ASR and average query numbers (Avg.Q) when attacking victim models on ImageNet for the “simple group” and “complex group”, respectively. For targeted attacks, we randomly set a target class (864) and 1,000 images correctly classified by the victim model, excluding those belonging to the target class, as the test set. It is demonstrated that on average (see the “Average” columns), our DifAttack++ surpasses all compared methods in both ASR and Avg.Q. More specifically, when compared with the second-best method in the challenging targeted attacks, i.e. MCGSquare, for the “simple group” (see Table 2), DifAttack++ reduces Avg.Q by 37.4% meanwhile improving the ASR by an average of 1%. Regarding results for “complex group” in Table 3, DifAttack++ achieves a higher ASR (1.1%) and decreases the Avg.Q from 3,733 to 2,619 (29.8% reduction). Similarly, in untargeted attacks, DifAttack++ diminishes the Avg.Q by 41.5% and 27.5% for the “complex group” and “simple group”, respectively, when compared with MCGSquare.

Besides the overall improvement of the attack efficiency and ASR, DifAttack++ also significantly outperforms MCGSquare in terms of the visual quality of AEs, making DifAttack++ less perceptible and more

practical. As can be seen from Fig. 2, AEs generated by MCGSquare results in severe visual distortions, e.g., colored blocks or stripes, which are due to the algorithmic characteristics of SquareAttack and MCGSquare. In fact, MCGSquare based on SquareAttack produces similar patterns of adversarial perturbations as SquareAttack does. More severely distorted AEs can be observed in [Andriushchenko et al \(2020\)](#). In contrast, our DifAttack++ crafts AEs with much subtle and imperceptible perturbations. This is because we effectively disentangle the visual and adversarial features of images, and ensure that images’ VFs remain almost unchanged during the generation of AEs, while updating only the AFs. Quantitatively, we also evaluate the similarity between AEs and their associated clean images for DifAttack++ and MCGSquare. From the results summarized in Table 4, we notice that the quality of AEs’ generated by DifAttack++ significantly surpasses that of MCGSquare for all considered metrics; e.g. over 2.5 dB gains in PSNR.

In addition to the above comparisons with SOTA attack methods, we would also like to compare with our early version DifAttack. From Tables 2-3, it can be seen that DifAttack++ outperforms DifAttack by big margins, in terms of ASR and query efficiency. Also, DifAttack++ greatly enhances the training efficiency and test stability. In Fig. 3, we depict the curve of test Avg.Q with respect to the training time, under untargeted attacks against four different victim models. As shown in Figs. 3(a) and (b), it is indicated that, generally, models trained by DifAttack++ converge faster. For example, when the victim model is EfficientNet-B3, using an NVIDIA RTX 3090 GPU and a batch size of 16, DifAttack++ only requires 4 hours to obtain two well-trained autoencoders, whereas DifAttack takes approximately 1 day. Additionally, DifAttack is more likely to overfit to surrogate models, as DifAttack leads to a gradual increase in the test Avg.Q with the prolongation of training time, as depicted in Fig. 3(c). In contrast, DifAttack++ demonstrates more stable attack performance with smaller oscillations, as illustrated in Fig. 3(a)-(d).

#### 4.3 The Open-set Scenario

The experiments above confirm that in closed-set scenarios, DifAttack++ achieves superior ASR and query efficiency compared to SOTA methods, while still maintaining high visual quality of AEs. In this subsection, we further evaluate the attack performance in the more challenging open-set scenarios, where the victim model’s training set could differ from those of surrogate models. Here, we consider the challenging task of

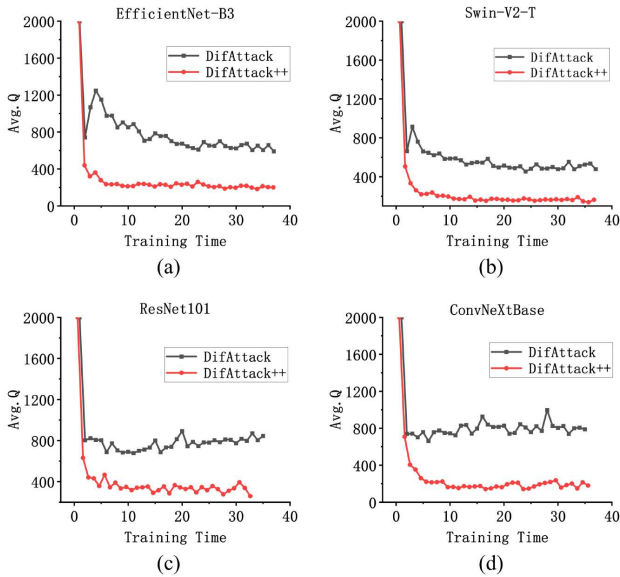


Fig. 3: The test Avg.Q with respect to the training time, when using DifAttack or DifAttack++ to perform untargeted attacks on ImageNet.

attacking CLIP models trained on large-scale datasets and a real-world API with unknown training data.

#### 4.3.1 Black-box Attacks against CLIP models

Taking the untargeted attack as an example, we generate AEs for test images from Food101 and ObjectNet datasets to attack their corresponding CLIP models. The employed surrogate models are Swin-V2-T, ConvNeXtBase, and ResNet101 pretrained on ImageNet. As shown in Table 5, it is worth noting that we only evaluate attack methods applicable for such an open-set scenario. The results demonstrate that DifAttack++ achieves significant improvements in ASR and Avg.Q over other black-box methods, especially when the victim model and classification task are relatively complicated, e.g. classification on ObjectNet via ViT-H-14-CLIPA-336 model. In fact, both methods based on feature disentanglement, namely, DifAttack and DifAttack++ perform satisfactorily, with DifAttack++ showing further improvements in query efficiency.

#### 4.3.2 Black-box Attacks against Real-world API

To evaluate the attack performance in a more practical open-set scenario, we assess comparative methods by attacking the real-world Imagga API Imagga (2024). This API utilizes a recognition model trained on a diverse dataset of daily images spanning over 3,000 unknown categories. The Imagga provides multiple predicted classes and corresponding scores for each

Table 5: The ASR and Avg.Q in untargeted attacks against CLIP models.

Datasets→	Food101		ObjectNet		
	Methods↓	ASR	Avg.Q	ASR	Avg.Q
	SimBA	100.0%	157	86.5%	2,636
	SignH	96.0%	1,139	90.0%	2,073
	$\mathcal{N}$ Attack	100.0%	342	100.0%	554
	NES	100.0%	614	96.5%	1,665
	DifAttack	100.0%	132	100.0%	239
	<b>DifAttack++</b>	<b>100.0%</b>	<b>84</b>	<b>100.0%</b>	<b>213</b>

Table 6: The ASR and Avg.Q when attacking real-world Imagga API.

Settings→	Untargeted		Targeted		
	Methods↓	ASR	Avg.Q	ASR	Avg.Q
	SignH	70.0	186.3	63.6	211.8
	Nattack	76.7	192.1	38.2	406.1
	SimBA	60.0	291.6	54.5	244.0
	GFCS	70.0	198.3	-	-
	MCGSquare	73.3	134.1	-	-
	DifAttack	80.0	132.2	68.2	196.8
	<b>DifAttack++</b>	<b>86.7</b>	<b>92.1</b>	<b>72.7</b>	<b>163.4</b>

query image. Due to the API’s call limits, we choose the top-performing six methods in the above experiments as the comparative methods, which are DifAttack, MCGSquare, CGA, GFCS, SimBA,  $\mathcal{N}$ Attack and SignH. We use the autoencoder and surrogate models pre-trained on ImageNet to extract disentangled features of test images from ImageNet. In untargeted attacks, we aim to remove the top 3 predicted classes of clean images; while in targeted attacks, we set the target class to be the second-highest scoring class among API’s predicted classes. The experimental results in Table 6 suggest that even when the actual training dataset is completely unknown, our DifAttack++ still exhibits superior ASR and Avg.Q simultaneously than comparative methods both in untargeted and targeted attacks. Notably, GFCS and MCGSquare successfully generate AEs in untargeted attacks but not in targeted attacks, since they are unable to craft AEs when the target class does not occur in the output of surrogate models.

#### 4.4 Black-box Attack against Defensive Methods

It is also important to evaluate the performance of attack methods against defensive strategies. We compare the ASR of comparative methods in untargeted attacks when encountering several SOTA defensive techniques, including Adversarially Training (AT) and pre-processing based methods, such as Bit-depth Reduction (Bit-Red) Xu et al (2018), Neural Representation Purifier (NRP) Naseer et al (2020) and Diffusion Pu-



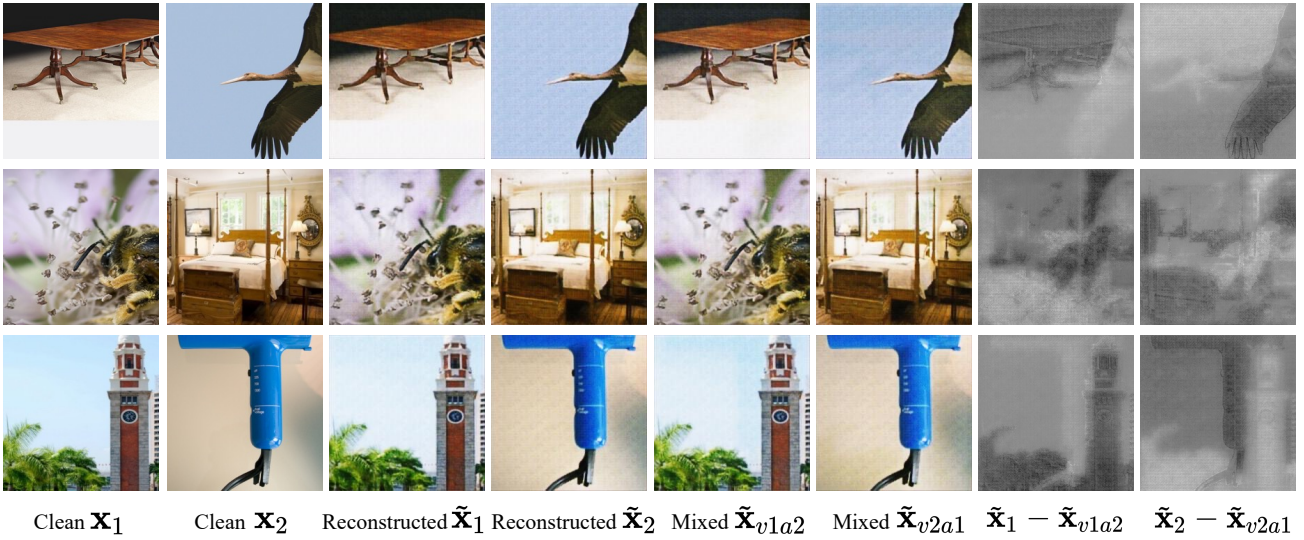


Fig. 4: The visualization of disentangled representation in DifAttack++. Images  $\tilde{x}_1$  and  $\tilde{x}_2$  are the reconstructed versions of  $x_1$  and  $x_2$  respectively by our pretrained autoencoder  $\mathcal{G}$ . The image  $\tilde{x}_{v1a2}$  is reconstructed by  $\mathcal{G}$  using the VFs of  $x_1$  and the AFs of  $x_2$ , while  $\tilde{x}_{v2a1}$  is reconstructed by  $\mathcal{G}$  using the VFs of  $x_2$  and the AFs of  $x_1$ .

rifier (DiffPure) Nie et al (2022). For attacking AT models pre-trained on ImageNet, we adopt adversarially trained ResNet-50 as the surrogate model and the more powerful classifier Wide-ResNet-50-2 as the victim model Salman et al (2020). For other defensive techniques, we use them to process AEs from ImageNet generated for attacking standardly trained ResNet-18, and then evaluate the ASR of these AEs after being processed. The experimental results shown in Table 7 showcase that our DifAttack++ achieves the highest average ASR against these four advanced defensive techniques, surpassing the second-place MCGSquare by nearly 10%. DifAttack++ is also the only method, among the comparative ones, with an average ASR exceeding 50%. Furthermore, DifAttack++ obtains two first places and two second places in terms of ASR. These results indicate that the AEs generated by DifAttack++ are more effective in resisting various types of defense mechanisms. Meanwhile, it demonstrates the ability of DifAttack++ to effectively decouple adversarial features from adversarially trained models.

Another interesting phenomenon is from Fig. 2, where we notice that the adversarial perturbations generated by MCGSquare consist mainly of colorful blocks; quite differ from conventional adversarial noise patterns. Consequently, MCGSquare exhibits desirable performance against the defense mechanism that focuses mainly on perturbations created by gradient-based attacks, e.g., the traditional AT, or DiffPure, which is more suitable for dealing with irregular adversarial noise patterns due to its diffusion process.

Table 7: The ASR of AEs from ImageNet against various SOTA defensive techniques in untargeted settings.

Methods	AT	BitRed	NRP	DiffPure	Avg.ASR
SignH	36.7	38.0	28.9	12.6	29.1
NES	18.6	21.0	31.3	20.0	22.7
$\mathcal{N}$ Attack	39.2	45.0	34.9	24.0	35.8
SimBA	39.5	14.5	25.8	13.1	23.2
BASES	0.0	58.5	28.5	8.6	23.9
P-RGF	43.2	38.0	37.5	30.4	37.3
Subspace	54.8	54.0	29.5	14.8	38.3
GFCS	6.8	21.5	32.9	22.5	20.9
MCGSquare	<b>70.5</b>	<b>72.0</b>	10.0	<b>65.5</b>	<b>49.2</b>
DifAttack	52.5	46.5	<b>41.5</b>	28.5	42.3
<b>DifAttack++</b>	<b>66.0</b>	<b>77.5</b>	<b>48.0</b>	<b>48.0</b>	<b>57.8</b>

#### 4.5 Analysis on Disentangled Features

To gain a more intuitive understanding of the characteristics of VFs and AFs disentangled by our method, we would like to observe the changes in reconstructed images by exchanging the VFs and AFs of a pair of images. Specifically, we first apply a well pre-trained autoencoder  $\mathcal{G}$  to reconstruct and disentangle clean images  $x_1$  and  $x_2$ , resulting in their respective reconstructed images ( $\tilde{x}_1$  and  $\tilde{x}_2$ ) along with their VFs and AFs. Next, we input  $x_1$ 's VFs and  $x_2$ 's AFs into the feature fusion layer  $\mathbf{M}$  of  $\mathcal{G}$ , obtaining the mixed image  $\tilde{x}_{v1a2}$ . Similarly, using  $x_1$ 's AFs and  $x_2$ 's VFs, we have  $\tilde{x}_{v2a1}$ .

As shown in Fig. 4, we randomly select three samples from the test dataset to visualize the above process. Notably, the visual quality of the reconstructed



Table 8: The ablation study on the usage of CD, the HDF module, the adoption of the initial image, and the number of disentanglement layers.

Victims	GoogleNet				ResNet18				VGG16				SqueezeNet				Average			
	Targeted		Untargeted		Targeted		Untargeted		Targeted		Untargeted		Targeted		Untargeted		Targeted		Untargeted	
Metrics	ASR	Avg.Q	ASR	Avg.Q	ASR	Avg.Q	ASR	Avg.Q	ASR	Avg.Q	ASR	Avg.Q	ASR	Avg.Q	ASR	Avg.Q	ASR	Avg.Q	ASR	Avg.Q
DifAttack	97.0%	3,201	100.0%	165	100.0%	1,901	100.0%	156	100.0%	2,246	100.0%	123	98.0%	2,793	100.0%	90	98.8%	2,535	100.0%	134
Dif+CD	98.0%	3,018	100.0%	177	100.0%	1,916	100.0%	137	100.0%	2,104	100.0%	53	99.0%	2,430	100.0%	78	99.3%	2,367	100.0%	111
Dif+CD+HDF	98.5%	2,847	100.0%	133	100.0%	1,685	100.0%	120	100.0%	1,825	100.0%	60	99.0%	2,242	100.0%	55	99.4%	2,150	100.0%	92
Dif+CD+HDF(3L)	98.5%	2,822	100.0%	137	100.0%	1,797	100.0%	116	100.0%	2,255	100.0%	58	99.5%	2,448	100.0%	85	99.5%	2,331	100.0%	99
<b>Dif+CD+HDF+<math>\hat{\mathbf{x}}_T</math></b>	<b>99.5%</b>	<b>1,530</b>	100.0%	<b>80</b>	100.0%	<b>957</b>	100.0%	<b>62</b>	100.0%	<b>969</b>	100.0%	<b>52</b>	<b>99.0%</b>	<b>1,389</b>	100.0%	<b>41</b>	<b>99.6%</b>	<b>1,211</b>	100.0%	<b>58</b>

images is predominantly influenced by VFs, with minimal impact from AFs. For instance, when the VFs used for reconstructing an image originate from  $\mathbf{x}_1$ , the reconstructed image (i.e.,  $\tilde{\mathbf{x}}_1$  and  $\tilde{\mathbf{x}}_{v1a2}$ ) closely resembles  $\mathbf{x}_1$  in visual quality, no matter where their AFs come from. Similarly, VFs from  $\mathbf{x}_2$  yield  $\tilde{\mathbf{x}}_2$  and  $\tilde{\mathbf{x}}_{v2a1}$ , which closely resemble  $\mathbf{x}_2$ . On the other hand, by observing the residual in reconstructed images when only AFs are replaced while keeping VFs unaltered (i.e.,  $\tilde{\mathbf{x}}_1 - \tilde{\mathbf{x}}_{v1a2}$  and  $\tilde{\mathbf{x}}_2 - \tilde{\mathbf{x}}_{v2a1}$ ), we find that AFs significantly impact the region of category-specific objects in the reconstructed images, akin to the classifier’s attention. For example, in the first row, when  $\tilde{\mathbf{x}}_{v1a2}$ ’s AFs come from  $\mathbf{x}_2$ , the residual image  $\tilde{\mathbf{x}}_1 - \tilde{\mathbf{x}}_{v1a2}$  focuses on the “black stork” object, which corresponds to the brightest area (large pixel values) in the image  $\tilde{\mathbf{x}}_1 - \tilde{\mathbf{x}}_{v1a2}$ . Conversely, when  $\tilde{\mathbf{x}}_{v2a1}$ ’s AFs come from  $\mathbf{x}_1$ , the changes concentrate on the “dining table” object (highlighted in  $\tilde{\mathbf{x}}_2 - \tilde{\mathbf{x}}_{v2a1}$ ). Such a phenomenon can also be similarly observed in the other two rows.

Based on the experimental results and analysis above, we can draw two conclusions: 1) Our DifAttack++ is capable of effectively disentangling VFs and AFs of images, and 2) VFs primarily determine the visual quality of images, and are mainly dependent on images’ signals themselves, while AFs are more associated with the attention regions of the classifier and relatively independent of images’ signals.

#### 4.6 Ablation Studies

We now conduct ablation experiments on the number of disentanglement layers in HDF and three key modules introduced in our proposed DifAttack++ (relative to our early version DifAttack). Specifically, These three modules are 1) CD: the training stage transitioned from using a single autoencoder for both clean images and AEs to two separate autoencoders for clean and adversarial domains, i.e. cross-domain; 2) HDF: the disentanglement module within the autoencoder changed from a single-layer DF module to a two-layer HDF module; and 3)  $\hat{\mathbf{x}}_T$ : the initial images at the attack stage shifted from clean samples to transferable AEs in close-set scenar-

ios, namely from  $\mathbf{x}$  to  $\hat{\mathbf{x}}_T$  generated by SI-NI-TI-DIM. The evaluation results are summarized in Table 8. To assess the advantages of CD, we maintain the autoencoder architecture used in DifAttack and retain clean initial images, while adopting two autoencoders responsible for clean and adversarial domains separately, denoted as Dif+CD. Subsequently, to evaluate the HDF, we replace the DF in each autoencoder of Dif+CD with HDF, denoted as Dif+CD+HDF. To measure the gain of transferable AEs, we replace the clean initial images  $\mathbf{x}$  in Dif+CD+HDF with the AE  $\hat{\mathbf{x}}_T$ , representing our ultimate DifAttack++ used in closed-set scenarios. In addition, to further examine the influence of the increasing number of disentanglement layers, we add an extra disentanglement layer behind “Disentanglement layer 2” in Fig. 1(a), while keeping other training and attack schemes the same with Dif+CD+HDF (two layers). The additional layer disentangles input features into AFs and VFs and then fuses these AFs and VFs before feeding them to  $\mathbf{M}_v/\mathbf{M}_a/\mathbf{M}_v^*/\mathbf{M}_a^*$ . This comparative module is designated as “Dif+CD+HDF(3L)”.

Table 8 shows that the three new modules proposed in DifAttack++ effectively enhance the average ASR and query efficiency simultaneously when attacking four different victim models in both targeted and untargeted attacks. By noticing the rows of “DifAttack” and “Dif+CD”, we see that incorporating CD leads to a 0.5% increase in the average targeted ASR while reducing the average Avg.Q by 6.6%. Also, upon the introduction of the HDF, i.e. from “Dif+CD” to “Dif+CD+HDF”, the average targeted ASR improves by 0.1% while the average Avg.Q decreases by 9.2%. Besides,  $\hat{\mathbf{x}}_T$  also brings nearly 1,000 (from 2,150 to 1,211) reduction in terms of average targeted Avg.Q. As the untargeted attack is a relatively simpler task compared to the targeted attack and DifAttack already achieves a 100% ASR and an Avg.Q of around 100, the enhancement effects of various modules on untargeted attacks fluctuate slightly across different victim models. But on average, the settings of CD, HDF, and  $\hat{\mathbf{x}}_T$  still reduce the average Avg.Q by 23/19/34, respectively. Moreover, we observe that more layers of disentanglement do not necessarily result in better performance. A comparison between “Dif+CD+HDF” and

“Dif+CD+HDF(3L)” reveals that introducing a third layer not only increases model parameters but also provides limited performance improvement. For instance, although the average ASR in the untargeted and targeted attacks remains stable or slightly increases by 0.1%, the average Avg.Q remains comparable and does not decrease noticeably. This may be because two disentanglement layers are already adequate for the current dataset and classification task, while additional layers could potentially lead to the model overfitting.

## 5 Conclusion

This work presents a novel query-efficient score-based black-box adversarial attack method named DifAttack++, which aims to hierarchically disentangle the adversarial and visual features from an image’s latent feature and perform black-box attacks via the disentangled feature space in cross-domain. The main idea is to optimize the adversarial feature while keeping the visual feature unchanged until a successful AE is obtained. Experimental results demonstrate the superior attack efficiency of DifAttack++ in both close-set and open-set scenarios, meanwhile maintaining a satisfactory visual quality of AEs.

## References

- Achille A, Soatto S (2018) Information dropout: Learning optimal representations through noisy computation. *IEEE Trans Pattern Anal Mach Intell* 40(12):2897–2905
- Al-Dujaili A, O’Reilly UM (2020) Sign bits are all you need for black-box attacks. In: *Proc. Int. Conf. Learn. Represent.*
- Andriushchenko M, Croce F, Flammarion N, Hein M (2020) Square attack: a query-efficient black-box adversarial attack via random search. In: *Proc. Eur. Conf. Comput. Vis.*, Springer, pp 484–501
- Barbu A, Mayo D, Alverio J, Luo W, Wang C, Gutfreund D, Tenenbaum J, Katz B (2019) Objectnet: A large-scale bias-controlled dataset for pushing the limits of object recognition models. In: *Proc. Adv. Neural Inf. Process. Syst.*, vol 32
- Bengio Y, Courville A, Vincent P (2013) Representation learning: A review and new perspectives. *IEEE Trans Pattern Anal Mach Intell* 35(8):1798–1828
- Bossard L, Guillaumin M, Van Gool L (2014) Food-101—mining discriminative components with random forests. In: *Proc. Eur. Conf. Comput. Vis.*, Springer, pp 446–461
- Brendel W, Rauber J, Bethge M (2018) Decision-based adversarial attacks: Reliable attacks against black-box machine learning models. In: *Proc. Int. Conf. Learn. Represent.*
- Burgess CP, Higgins I, Pal A, Matthey L, Watters N, Desjardins G, Lerchner A (2018) Understanding disentangling in beta-VAE. *arXiv preprint arXiv:1804.03599*
- Cai R, Li Z, Wei P, Qiao J, Zhang K, Hao Z (2019) Learning disentangled semantic representation for domain adaptation. In: *Int. Joint Conf. Artif. Intell.*, NIH Public Access, vol 2019, p 2060
- Cai Z, Song C, Krishnamurthy S, Roy-Chowdhury A, Asif S (2022) Blackbox attacks via surrogate ensemble search. In: *Proc. Adv. Neural Inf. Process. Syst.*, vol 35, pp 5348–5362
- Carlini N, Wagner D (2017) Towards evaluating the robustness of neural networks. In: *Proc. IEEE Symp. Secur. Priv.*, pp 39–57
- Chen H, Zhang Y, Wu S, Wang X, Duan X, Zhou Y, Zhu W (2024) Disenbooth: Identity-preserving disentangled tuning for subject-driven text-to-image generation. In: *Proc. Int. Conf. Learn. Represent.*
- Cheng S, Dong Y, Pang T, Su H, Zhu J (2019) Improving black-box adversarial attacks with a transfer-based prior. In: *Proc. Adv. Neural Inf. Process. Syst.*, vol 32
- Croce F, Hein M (2020a) Minimally distorted adversarial examples with a fast adaptive boundary attack. In: *Proc. Int. Conf. Mach. Learn.*, pp 2196–2205
- Croce F, Hein M (2020b) Reliable evaluation of adversarial robustness with an ensemble of diverse parameter-free attacks. In: *Proc. Int. Conf. Mach. Learn.*, pp 2206–2216
- Deng J, Dong W, Socher R, Li LJ, Li K, Fei-Fei L (2009) Imagenet: A large-scale hierarchical image database. In: *Proc. IEEE Conf. Comput. Vis. Pattern Recognit.*, IEEE, pp 248–255
- Dong Y, Liao F, Pang T, Su H, Zhu J, Hu X, Li J (2018) Boosting adversarial attacks with momentum. In: *Proc. IEEE Conf. Comput. Vis. Pattern Recognit.*, pp 9185–9193
- Dong Y, Fu QA, Yang X, Pang T, Su H, Xiao Z, Zhu J (2020) Benchmarking adversarial robustness on image classification. In: *Proc. IEEE Conf. Comput. Vis. Pattern Recognit.*, pp 321–331
- Du J, Zhang H, Zhou JT, Yang Y, Feng J (2020) Query-efficient meta attack to deep neural networks. In: *Proc. Int. Conf. Learn. Represent.*
- Feng Y, Wu B, Fan Y, Liu L, Li Z, Xia ST (2022) Boosting black-box attack with partially transferred conditional adversarial distribution. In: *Proc. IEEE Conf. Comput. Vis. Pattern Recognit.*, pp 15095–15104

- Gadre SY, Ilharco G, Fang A, Hayase J, Smyrnis G, Nguyen T, Marten R, Wortsman M, Ghosh D, Zhang J, et al (2024) Datacomp: In search of the next generation of multimodal datasets. In: *Proc. Adv. Neural Inf. Process. Syst.*, vol 36
- Gonzalez-Garcia A, Van De Weijer J, Bengio Y (2018) Image-to-image translation for cross-domain disentanglement. In: *Proc. Adv. Neural Inf. Process. Syst.*, vol 31
- Google (2024) Google cloud vision api. “<https://cloud.google.com/vision>”, accessed:2024-06-07
- Guo C, Rana M, Cisse M, van der Maaten L (2018) Countering adversarial images using input transformations. In: *Proc. Int. Conf. Learn. Represent.*
- Guo C, Gardner J, You Y, Wilson AG, Weinberger K (2019a) Simple black-box adversarial attacks. In: *Proc. Int. Conf. Mach. Learn.*, pp 2484–2493
- Guo Y, Yan Z, Zhang C (2019b) Subspace attack: Exploiting promising subspaces for query-efficient black-box attacks. In: *Proc. Adv. Neural Inf. Process. Syst.*, vol 32
- Huang Z, Zhang T (2020) Black-box adversarial attack with transferable model-based embedding. In: *Proc. Int. Conf. Learn. Represent.*
- Ilharco G, Wortsman M, Wightman R, Gordon C, Carlini N, Taori R, Dave A, Shankar V, Namkoong H, Miller J, Hajishirzi H, Farhadi A, Schmidt L (2021) Openclip. URL [https://github.com/mlfoundations/open\\_clip](https://github.com/mlfoundations/open_clip)
- Ilyas A, Engstrom L, Athalye A, Lin J (2018) Black-box adversarial attacks with limited queries and information. In: *Proc. Int. Conf. Mach. Learn.*, pp 2137–2146
- Imagga (2024) Ai-powered image tagging api. “<https://imagga.com/solutions/auto-tagging>”, accessed:2024-06-07
- Kazemi E, Kerdreux T, Wang L (2023) Minimally distorted structured adversarial attacks. *Int J Comput Vis* 131(1):160–176
- Kim H, Mnih A (2018) Disentangling by factorising. In: *Proc. Int. Conf. Mach. Learn.*, pp 2649–2658
- Kim J, Lee BK, Ro YM (2021) Distilling robust and non-robust features in adversarial examples by information bottleneck. In: *Proc. Adv. Neural Inf. Process. Syst.*, vol 34, pp 17148–17159
- Lee HY, Tseng HY, Mao Q, Huang JB, Lu YD, Singh MK, Yang MH (2020) Drit++: Diverse image-to-image translation via disentangled representations. *Int J Comput Vis* pp 1–16
- Li P, Pei Y, Li J (2023) A comprehensive survey on design and application of autoencoder in deep learning. *Appl Soft Comput* p 110176
- Li Y, Li L, Wang L, Zhang T, Gong B (2019) Nat-tack: Learning the distributions of adversarial examples for an improved black-box attack on deep neural networks. In: *Proc. Int. Conf. Mach. Learn.*, pp 3866–3876
- Li Y, Hu L, Dong L, Wu H, Tian J, Zhou J, Li X (2024) Transformer-based image inpainting detection via label decoupling and constrained adversarial training. *IEEE Trans Circuits Syst Video Technol* 34(3):1857–1872
- Lin CC, Chu HL, Wang YCF, Lei CL (2021) Joint feature disentanglement and hallucination for few-shot image classification. *IEEE Trans Image Process* 30:9245–9258
- Lin J, Song C, He K, Wang L, Hopcroft JE (2019) Nesterov accelerated gradient and scale invariance for adversarial attacks. In: *Proc. Int. Conf. Learn. Represent.*
- Lin WA, Lau CP, Levine A, Chellappa R, Feizi S (2020) Dual manifold adversarial robustness: Defense against lp and non-lp adversarial attacks. In: *Proc. Adv. Neural Inf. Process. Syst.*, vol 33, pp 3487–3498
- Liu J, Zhou J, Wu H, Sun W, Tian J (2023) Generating robust adversarial examples against online social networks (osns). *ACM Trans Multimedia Comput Commun Appl* 20(4)
- Liu J, Zhou J, Tian J, Sun W (2024a) Recoverable privacy-preserving image classification through noise-like adversarial examples. *ACM Trans Multimedia Comput Commun Appl* 20(7)
- Liu J, Zhou J, Zeng J, Tian J (2024b) Difattack: Query-efficient black-box attack via disentangled feature space. In: *Proc. AAAI Conf. Artif. Intell.*, vol 38, pp 3666–3674
- Lord NA, Mueller R, Bertinetto L (2022) Attacking deep networks with surrogate-based adversarial black-box methods is easy. In: *Proc. Int. Conf. Learn. Represent.*
- Lu S, Xian Y, Yan K, Hu Y, Sun X, Guo X, Huang F, Zheng WS (2021) Discriminator-free generative adversarial attack. In: *Proc. ACM Int. Conf. Multimedia.*, pp 1544–1552
- Ma C, Chen L, Yong JH (2021) Simulating unknown target models for query-efficient black-box attacks. In: *Proc. IEEE Conf. Comput. Vis. Pattern Recognit.*, pp 11835–11844
- Ma X, Kong X, Zhang S, Hovy EH (2020) Decoupling global and local representations via invertible generative flows. In: *Proc. Int. Conf. Learn. Represent.*
- Madry A, Makelov A, Schmidt L, Tsipras D, Vladu A (2018) Towards deep learning models resistant to adversarial attacks. In: *Proc. Int. Conf. Learn. Represent.*
- Meo C, Mahon L, Goyal A, Dauwels J (2024) atc-vae: On the relationship between disentanglement and di-

- versity. In: *Proc. Int. Conf. Learn. Represent.*
- Mohaghegh Dolatabadi H, Erfani S, Leckie C (2020) Advflow: Inconspicuous black-box adversarial attacks using normalizing flows. In: *Proc. Adv. Neural Inf. Process. Syst.*, pp 15871–15884
- Mustafa A, Khan SH, Hayat M, Goecke R, Shen J, Shao L (2020) Deeply supervised discriminative learning for adversarial defense. *IEEE Trans Pattern Anal and Mach Intell* 43(9):3154–3166
- Naseer M, Khan S, Hayat M, Khan FS, Porikli F (2020) A self-supervised approach for adversarial robustness. In: *Proc. IEEE Conf. Comput. Vis. Pattern Recognit.*, pp 262–271
- Nie Q, Liu Y (2021) View transfer on human skeleton pose: Automatically disentangle the view-variant and view-invariant information for pose representation learning. *Int J Comput Vis* 129(1):1–22
- Nie W, Guo B, Huang Y, Xiao C, Vahdat A, Anandkumar A (2022) Diffusion models for adversarial purification. In: *Proc. Int. Conf. Mach. Learn.*
- Peng X, Huang Z, Sun X, Saenko K (2019) Domain agnostic learning with disentangled representations. In: *Proc. Int. Conf. Mach. Learn.*, PMLR, pp 5102–5112
- Pope P, Zhu C, Abdelkader A, Goldblum M, Goldstein T (2020) The intrinsic dimension of images and its impact on learning. In: *Proc. Int. Conf. Learn. Represent.*
- Qin Y, Xiong Y, Yi J, Hsieh CJ (2023) Training meta-surrogate model for transferable adversarial attack. In: *Proc. AAAI Conf. Artif. Intell.*, vol 37, pp 9516–9524
- Qing Y, Bai T, Liu Z, Moulin P, Wen B (2024) Detection of adversarial attacks via disentangling natural images and perturbations. *IEEE Trans Inf Forensics Secur*
- Salman H, Ilyas A, Engstrom L, Kapoor A, Madry A (2020) Do adversarially robust imagenet models transfer better? In: *Proc. Adv. Neural Inf. Process. Syst.*, vol 33, pp 3533–3545
- Shao R, Perera P, Yuen PC, Patel VM (2022) Open-set adversarial defense with clean-adversarial mutual learning. *Int J Comput Vis* 130(4):1070–1087
- Stutz D, Hein M, Schiele B (2019) Disentangling adversarial robustness and generalization. In: *Proc. IEEE Conf. Comput. Vis. Pattern Recognit.*, pp 6976–6987
- Tian J, Zhou J, Li Y, Duan J (2021) Detecting adversarial examples from sensitivity inconsistency of spatial-transform domain. In: *Proc. AAAI Conf. Artif. Intell.*, vol 35, pp 9877–9885
- Vaze S, Han K, Vedaldi A, Zisserman A (2021) Open-set recognition: A good closed-set classifier is all you need. In: *Proc. Int. Conf. Learn. Represent.*
- Wang S, Nepal S, Rudolph C, Grobler M, Chen S, Chen T, An Z (2021) Defending adversarial attacks via semantic feature manipulation. *IEEE Trans Serv Comput* 15(6):3184–3197
- Wang X, Chen H, Tang S, Wu Z, Zhu W (2022) Disentangled representation learning. *arXiv preprint arXiv:221111695*
- Wei Z, Yang X, Wang N, Gao X (2023) Dual-adversarial representation disentanglement for visible infrared person re-identification. *IEEE Trans Inf Forensics Secur*
- Wierstra D, Schaul T, Glasmachers T, Sun Y, Peters J, Schmidhuber J (2014) Natural evolution strategies. *J Mach Learn Res* 15(1):949–980
- Wu H, Zhou J, Tian J, Liu J, Qiao Y (2022) Robust image forgery detection against transmission over online social networks. *IEEE Trans Inf Forensics Secur* 17:443–456
- Xu W, Evans D, Qi Y (2018) Feature squeezing: Detecting adversarial examples in deep neural networks. In: *NDDS Symp.*
- Yang S, Guo T, Wang Y, Xu C (2021) Adversarial robustness through disentangled representations. In: *Proc. AAAI Conf. Artif. Intell.*, vol 35, pp 3145–3153
- Yang T, Wang Y, Lu Y, Zheng N (2024) Disdiff: Un-supervised disentanglement of diffusion probabilistic models. In: *Proc. Adv. Neural Inf. Process. Syst.*, vol 36
- Yin F, Zhang Y, Wu B, Feng Y, Zhang J, Fan Y, Yang Y (2023) Generalizable black-box adversarial attack with meta learning. *IEEE Trans Pattern Anal and Mach Intell*
- Zhang H, Avrithis Y, Furon T, Amsaleg L (2021) Walking on the edge: Fast, low-distortion adversarial examples. *IEEE Trans Inf Forensics Secur* 16:701–713
- Zheng M, Yan X, Zhu Z, Chen H, Wu B (2023) Black-boxbench: A comprehensive benchmark of black-box adversarial attacks. *arXiv preprint arXiv:231216979*
- Zheng M, Yan X, Zhu Z, Chen H, Wu B (2024) Black-boxbench leaderboard. “<https://blackboxbench.github.io/leaderboard-imagenet.html>”, accessed:2024-06-07
- Zhu JY, Park T, Isola P, Efros AA (2017) Unpaired image-to-image translation using cycle-consistent adversarial networks. In: *Proc. IEEE Conf. Comput. Vis.*